

Alignment of Nematic Liquid Crystal 5CB Using Graphene Oxide

Grazia Giuseppina Politano ^{1,*}, Francesco Filice ² and Carlo Versace ^{2,3}

¹ Department of Information Engineering, Infrastructures and Sustainable Energy (DIIES), University “Mediterranea” of Reggio Calabria, 89122 Reggio Calabria, Italy

² Department of Physics, University of Calabria, 87036 Rende, Italy; carlo.versace@fis.unical.it (C.V.)

³ Licryl CNR/Nanotec c/o, Department of Physics, University of Calabria, 87036 Rende, Italy

* Correspondence: grazia.politano@unirc.it

Abstract: In this article, we employed the saturation voltage method (SVM) to investigate the interaction between a nematic liquid crystal (NLC) and a graphene oxide (GO) substrate. The SVM approach involved applying a potential difference (ΔV) to the cell containing the NLC (specifically, 5CB) to reorient the nematic director (n) from a parallel to a perpendicular configuration with respect to the cell’s surface. By utilizing sandwich cells with indium–tin oxide semi-transparent electrodes covered by GO, we measured the anchoring energy between the NLC and the thin GO film. To evaluate the strength of this anchoring energy, we compared the results with two other cells: one exhibiting strong anchoring energy (polyimide cell) and the other demonstrating weak anchoring energy (formvar cell). The influence of GO thin films on the alignment of nematic 5CB was distinctly observed.

Keywords: graphene oxide; nematic liquid crystals; surface anchoring energy

1. Introduction

Graphene has emerged as a material of great interest in the scientific community due to its exceptional properties and numerous applications [1–3]. Recent advancements in the field of metamaterials have highlighted the potential of graphene-based hyperbolic metamaterials, especially in the mid-IR frequency range [4]. However, despite its potential, there are challenges associated with graphene [5]. The issues of low-throughput production and high costs, particularly for high-quality CVD graphene, hinder its widespread industrial use [5]. Given these challenges, researchers have been exploring potential alternatives to traditional graphene [6].

Graphene oxide (GO) has emerged as a promising contender in this regard [7]. It is obtained by oxidizing graphite using strong oxidizing agents, leading to the insertion of various oxidized functionalities in the graphite structure [8]. These functionalities increase layer separation and make the material hydrophilic. GO can be exfoliated in water through sonication, resulting in single- or few-layer graphene-like structures. Due to disrupted conjugated electronic structures caused by the presence of oxidized functional groups, GO differs from graphene in that it possesses insulating properties, leading to irreversible defects and disorders [9]. GO finds use in several applications, including electronics, photonics, sensors, photocatalysis, and biomedicine [10–18].

Studies have delved into the potential of GO in the field of liquid crystals [19,20]. Abedin et al. [21] explored graphene oxide liquid crystals (GOLCs). Using high-speed shearing of graphite oxide, GOLCs were exfoliated in various solvents such as water, ethylene glycol, NMP, and DMF. Polarized light imaging became a pivotal tool in studying the equilibrium nematic phases of these lyotropic GOLCs, offering a deep dive into aggregation and textural features like domain size (d). Notably, in solvents like water and ethylene glycol, GOLCs exhibited large nematic domains surpassing 100 μm , marked by a high



Citation: Politano, G.G.; Filice, F.; Versace, C. Alignment of Nematic Liquid Crystal 5CB Using Graphene Oxide. *Crystals* **2023**, *13*, 1500. <https://doi.org/10.3390/cryst13101500>

Academic Editor: Benoit Heinrich

Received: 8 September 2023

Revised: 5 October 2023

Accepted: 12 October 2023

Published: 15 October 2023



Copyright: © 2023 by the authors. Licensee MDPI, Basel, Switzerland. This article is an open access article distributed under the terms and conditions of the Creative Commons Attribution (CC BY) license (<https://creativecommons.org/licenses/by/4.0/>).

degree of order. This stands in contrast to solvents like NMP and DMF, which presented domains in the range of 5 to 50 μm at analogous volume fractions.

While the exploration of GOLCs offers intriguing insights, the broader field of nematic liquid crystals (NLCs) remains central to our discussion. NLCs have found widespread applications in various technologies, such as displays, smart windows, light valves, and spatial light modulators [22]. NLC behavior is significantly influenced by their surface properties—particularly the surface anchoring energy, which holds a crucial role in the field of liquid crystal research [23].

Numerous scientists have devoted their efforts to studying these surface properties in recent years, resulting in valuable models and precise experimental techniques. These advancements have led to significant improvements in NLC display technology [24]. The bulk properties of NLC cells rely heavily on their surface regions, which are firmly anchored to the cell boundary substrates and do not undergo reorientation under normal operating voltage. These surface regions can only be reoriented under very intense electric fields, making the surface anchoring energy the measure of work required to reorient the NLC's surface region toward the bulk director orientation [23].

Due to the unique electronic properties of graphene, researchers have been actively investigating the interactions between NLCs and graphene. One noteworthy discovery [25] is the transformative effect of monolayer graphene films, which induce a planar alignment on the LC; this results in the emergence of pseudo-nematic domains (PNDs) at the interface of graphene. When immersed in a graphene-nematic mixture, these PNDs amplify the orientational order parameter, showcasing a remarkable augmentation in the LC's dielectric anisotropy. The interplay of these anisotropic domains with an external electric field even engenders a non-zero dielectric anisotropy within the isotropic phase. Moreover, the same study [25] unveils another intriguing facet: the incorporation of graphene flakes within the LC introduces a reduction in the concentration of free ions via a distinctive ion-trapping mechanism. This decline in mobile ions within the LC exerts a subsequent influence on the LC's rotational viscosity, facilitating a swifter response of the nematic director when the electric field is toggled on and off.

Graphene's potential extends beyond just interactions with NLCs. It can serve as both electrodes and aligning layers in liquid crystal devices, enhancing their performance [26]. Traditional NLC cells use polyimide-coated surfaces [27] with unidirectional rubbing to determine the NLC's nematic director profile. NLC molecules can form stable anchoring to the honeycomb pattern of graphene through π - π electron stacking interactions, driven by the overlap of the NLC's benzene rings on the graphene's honeycomb structure [25]. This interaction ensures that the NLC achieves a uniform planar-aligned state over a large-scale dimension on graphene [25]. The hexagonal graphene lattice, with a C-C bond length of 1.42 \AA , closely mirrors the hexagonal benzene ring with a C-C bond length of 1.40 \AA [26]. This near-identical size facilitates the coherent alignment of NLC molecules on the 2D graphene surface due to epitaxial interactions [28–30] between the benzene rings of the NLC molecules and the hexagonal lattice of graphene. This interaction is further characterized by the π - π electron stacking interaction with a binding energy ranging from 0.74 to 0.88 eV/molecule [31], which is attributed to a significant amount of charge transfer from the NLC molecule to the honeycomb pattern of the carbon atoms. Supporting this, the previous findings of Basu et al. [27,32,33] demonstrated that graphene can serve as the planar-alignment agent for an NLC due to this specific graphene-NLC interaction.

In addition to the aforementioned interactions, from a quantum chemical perspective, the π - π electron stacking between the benzene rings of the NLC and the graphene's honeycomb structure can be attributed to the overlap of their respective π orbitals. This overlap leads to a delocalization of electron density, further stabilizing the interaction and facilitating the alignment of the NLC molecules on the graphene surface.

Recent studies regarding the surface anchoring energy of NLC molecules on GO substrate have been carried out [34]. It is worth noting that NLCs can also interact with other types of materials under the influence of external fields. For example, a recent study [35]

introduced a new colloidal composite formed by specially synthesized dimethylphenyl ferrite particles and a nematic liquid crystal; it also discussed an in-depth exploration of anchoring energy.

Herein, we employed the saturation voltage method (SVM) to investigate the interaction between a liquid crystal and a GO substrate [23]. The approach involved applying a potential difference ΔV to the cell containing the nematic liquid crystal (in this case, 5CB) to reorient the nematic director n from a parallel ($//$) to a perpendicular (\perp) configuration with respect to the cell's surface. The suggested methodology is versatile and can be applied to liquid crystalline devices functioning in both the GHz and THz spectra. This advancement holds the potential to enhance the performance of existing transducers [36,37]. While SVM provides insights into the anchoring energy, it might not offer a complete understanding of all the interactions at play, necessitating complementary methods for a more comprehensive view.

We measured the anchoring energy between the NLC and a thin GO film. The study was conducted using sandwich cells with indium–tin oxide semi-transparent electrodes covered by GO. To assess the strength of this anchoring energy, we compared the results with two other cells, one exhibiting strong anchoring energy (polyimide cell) and the other demonstrating weak anchoring energy (formvar cell). We observed a significant effect of GO thin films on the alignment of nematic 5CB. These findings suggest that GO could play a crucial role in shaping the behavior of NLCs, with potential implications for various applications.

2. Materials and Methods

For the construction of the cells, two glass slides with pre-deposited indium–tin oxide (ITO) are prepared. GO, bought from Sigma-Aldrich (4% in H_2O), is then applied onto these slides using the dip-coating technique. The slides are allowed to dry afterward, and a 36 μm -thick Mylar spacer is placed between them. This spacer serves to reduce the thickness of the liquid crystal layer. The subsequent step involves creating contacts on the cell, where a potential difference will be applied. Finally, the nematic liquid crystal 5CB is introduced into the cell. The microscopic view of the cell containing 5CB, taken between crossed polarizers, is reported in Figure 1.

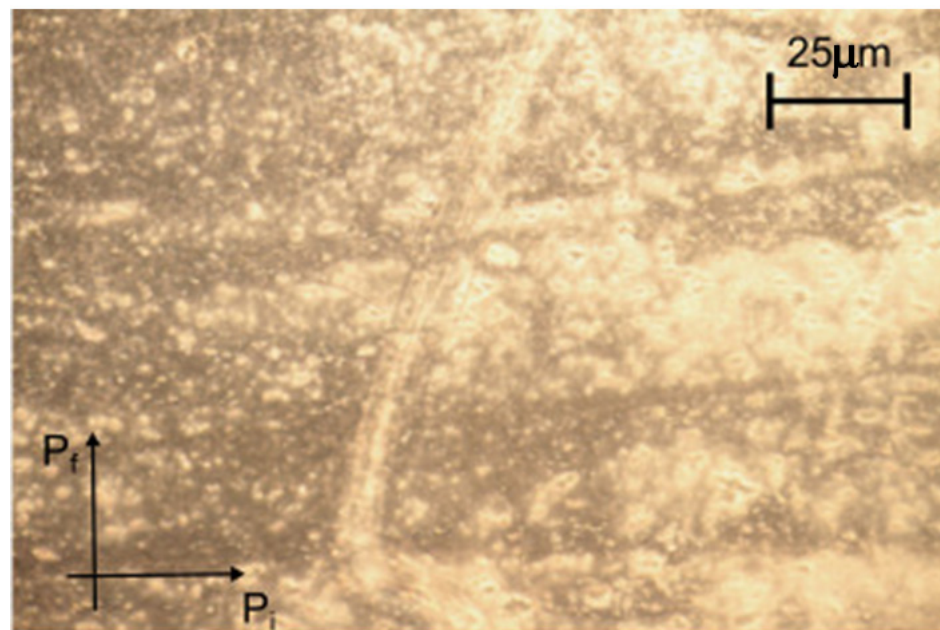


Figure 1. Microscopic view of the cell containing 5CB. The image was captured using a 10 \times objective lens. The polarizer angles are shown.

Figure 2 illustrates the schematic representation of the sandwich cell used in the study, while in the other two cells, we made variations by replacing GO with formvar and polyimide.

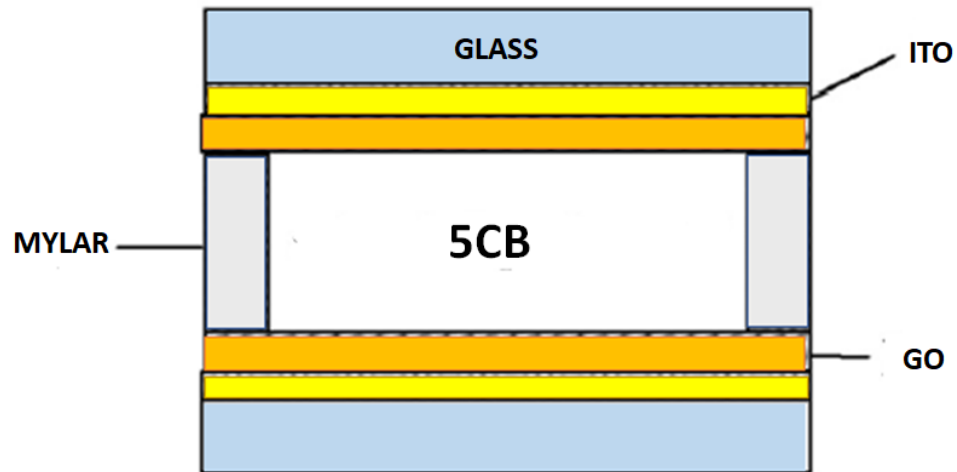


Figure 2. Schematic representation of the sandwich cell used in the study.

Formvar is a thermoplastic resin classified as a polyvinyl formal. It is derived from the polymerization of polyvinyl alcohol and formaldehyde, often co-polymerized with polyvinyl acetate. This resin is commonly employed in applications such as coatings, adhesives, and molding materials.

The polyimide cells were assembled with pretreated ITO glass slides purchased from EHC CO. Ltd. (Tokyo, Japan).

The Zeiss Axioskop was employed as a polarizing microscope and equipped with the following objectives: Plan-Neofluar 10×/0.30 Ph1, Plan-Neofluar 20×/0.50 Ph2, Plan-Neofluar 40×/0.75 Ph2 Antireflective, Plan-Neofluar 63×/1.25 Oil Ph3, and Plan-Neofluar 100×/1.30 Oil Ph3. The microscope was equipped with a Bertrand lens, too.

For phase difference measurement between the two waves exiting the GO cell, both 0–5λ and 0–20λ ZEISS quartz-tilting compensators were used to measure the optical dephasing; all measurements were performed in white light.

To induce reorientation of the molecular director of the NCL and to prevent electric charge screen effects, a 10 kHz AC voltage was applied across the NLC layer. The external voltage was supplied by a Hewlett-Packard 34401A arbitrary signal generator and a Kepco Model 80 P 500 M voltage amplifier. The experimental setup is shown in Figure 3.

Figure 3b shows a schematic of the experimental apparatus. The light emitted by the halogen lamp (L) is linearly polarized by the polarizer (P_i) and is focused on the sample via the optical condenser (OC). The microscope's long focal length objective (O) collects the cone of light emerging from the sample. The analyzer (P_f) allows the formation of the conoscopic interference image on the focal plane of (O). Finally, the interference pattern is projected by the camera's CMOS sensor (CCD).

The initial configuration of the NLC cell is planar with the molecular director n at 45° to P_i . The two polarizers, P_i and P_f , are crossed, as shown in Figure 3a. In this condition, the birefringence is maximal; for white light, the intensity reaching the camera is also maximal. Due to the high order of interference, the isogyres cannot be observed. Not even isochromatics can be observed, as the sample thickness is too small.

The compensator C is inserted between the sample S and the analyzer P_f so that its fast axis C is perpendicular to n (Figure 3a). In this way, the optical delay introduced by the compensator is subtracted from that caused by the sample.

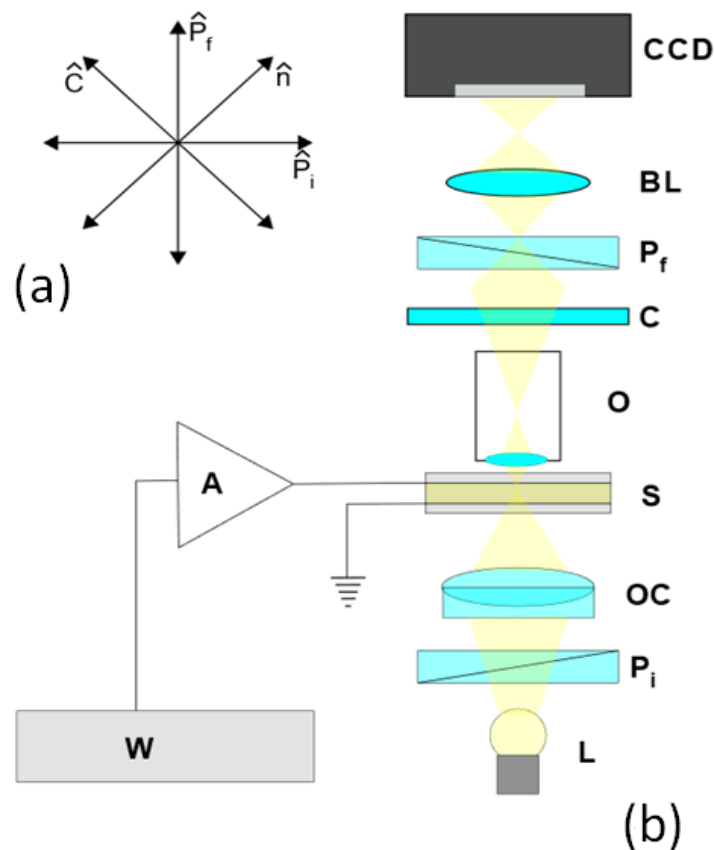


Figure 3. Experimental setup (a) relative orientation of the incident light polarization P_i , analyzer P_f , molecular director n , and fast axis of compensator C (b) W: waveform generator; A: amplifier; L: halogen lamp; P_i : polarizer; OC: optical condenser; S: liquid crystal sample; O: objective; C: tilting compensator; P_f : analyzer; BL: Bertrand lens; CMOS camera.

As the applied voltage exceeds the threshold voltage of the Fréedericksz transition, n begins to align with the applied electric field E . When n is almost fully aligned with E , the birefringence of the sample is small and isogyres can be observed.

By turning the compensator knob, the overall optical delay (sample + condenser) can be canceled. It is then possible to observe that the isogyres converge and come into contact when the delay is zero. The optical delay necessary to compensate for that introduced by the sample can be read directly on the compensator knob. The process is repeated by turning the compensator in the opposite direction and averaging the two measured delay values.

3. Results and Discussion

In this study, we use a generalized approach to describe the surface anchoring energy A , which involves evaluating interfacial energy using the SVM. SVM offers a promising proposal for standardizing anchoring energy measurements [23].

The SVM is based on the concept of saturation transition, which has been theoretically predicted by several scientists [38]. At the saturation voltage V_s , the director of the NLC demonstrates completely homeotropic alignment (i.e., perpendicular to the substrate), including the boundary layers. The anchoring strength A is connected to the saturation voltage V_s through the Sugimura relationship [39]:

$$A = \frac{V_s K_{22} \sqrt{\varepsilon_0 \Delta \varepsilon K_{33}}}{IK_{11}} \tanh \left(\frac{V_s}{2} \sqrt{\frac{\varepsilon_0 \Delta \varepsilon}{K_{33}}} \right) \quad (1)$$

Here, K_{11} , K_{22} , and K_{33} are the splay, twist, and bend elastic constants of the NLC, respectively. ϵ_0 represents the dielectric constant in space, while $\Delta\epsilon$ denotes the dielectric anisotropy of the liquid crystal. The parameter l stands for the thickness of the sample.

The remarkable aspect of the SVM is that it allows the complete determination of surface anchoring energy A without the need for additional numerical calculations. By knowing the saturation voltage V_s , we can directly calculate the surface anchoring energy using Equation (1). This approach presents a significant advancement in the standardization of anchoring energy measurement methods [23].

To calculate this voltage, we will require an alternating current generator with a frequency of 10 kHz (using such a high frequency ensures that the liquid crystal ions do not separate, creating potential wells within the cell). Additionally, a compensator is employed to measure the optical path difference (OPD) of our birefringent material.

The experimental setup involves placing the cell on the microscope and adjusting it until the optical axis of the microscope aligns perpendicularly (90 degrees). Then the initial orientation of the NLC director (easy axis) is determined with the help of the optical compensator by rotating the cell between the crossed polarizers; the fast axis of the compensator is positioned at 45° with respect to the easy axis. We have observed that the easy axis of the cell always coincided with the dipping direction. Subsequently, an AC voltage is applied to the cell to induce tilting of the liquid crystal, and data regarding the OPD are collected at various voltage levels.

In Figure 4 ΔL (OPD) vs. the inverse of the applied RMS voltage in the case of the sandwich cell using GO is reported.

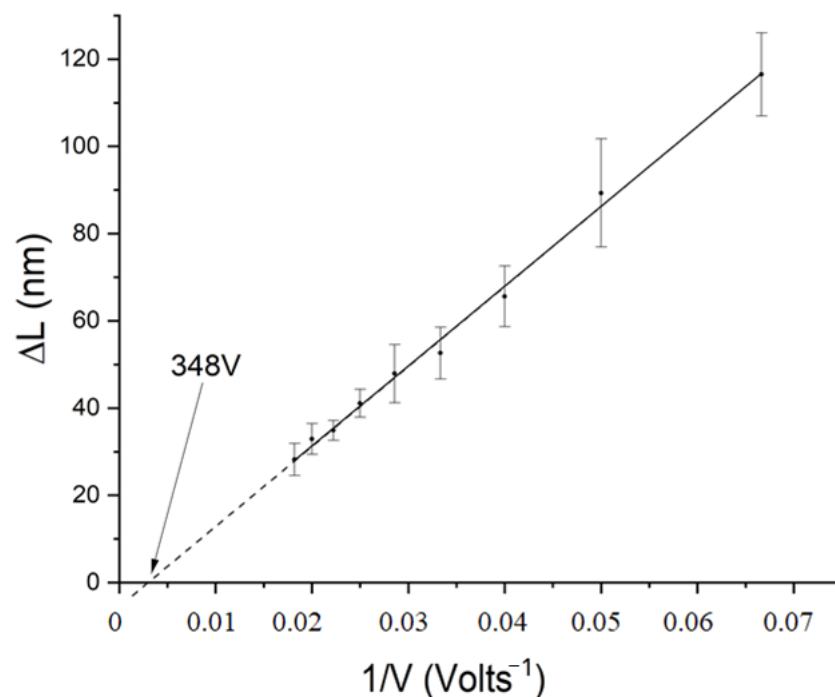


Figure 4. ΔL vs. the inverse of the applied RMS voltage in the case of the sandwich cell using graphene oxide. The linear fit of the experimental point (solid line) and the extrapolation (dashed line) is also shown. Each experimental point is the mean value of ten measurements made on different points of the sample. The y-error bar to each experimental point of the graph represents three times the standard deviation of the mean, while the x-error bar is negligible.

For an in-plane deformation of the director, OPD between the ray and the ordinary and extraordinary is defined as:

$$\Delta L = \int_0^h \sqrt{\frac{n_0^2 n_e^2}{n_e^2 \cos^2(\theta(z)) + n_0^2 \sin^2(\theta(z))}} dz - n_o h \quad (2)$$

where the z axis is normal to the cell surfaces; n_e and n_o are, respectively, the extraordinary and the ordinary refractive index of the nematic; h is the cell thickness; and $\theta(z)$ is the angle between the nematic director and the z axis. As the director is completely aligned along z , ΔL reduces to zero.

In our measurement, ΔL is read directly on the compensator wheel as the external voltage is increased.

The intrinsic structure of GO exhibits functional groups, including hydroxyls, epoxides, and carboxyls, attached to the basal planes and edges [40]. This unique configuration contributes to its strong interactions with NLC molecules. The π - π stacking interactions, specifically between the aromatic regions of NLC molecules and the conjugated system of GO, are pivotal in promoting alignment. The interaction due to π - π stacking is depicted in Figure 5, where the 5CB benzene rings are superimposed on the hexagonal GO structure. This pronounced π - π stacking interaction facilitates the 5CB's transition into a planar-aligned state across a broad scale on the GO.

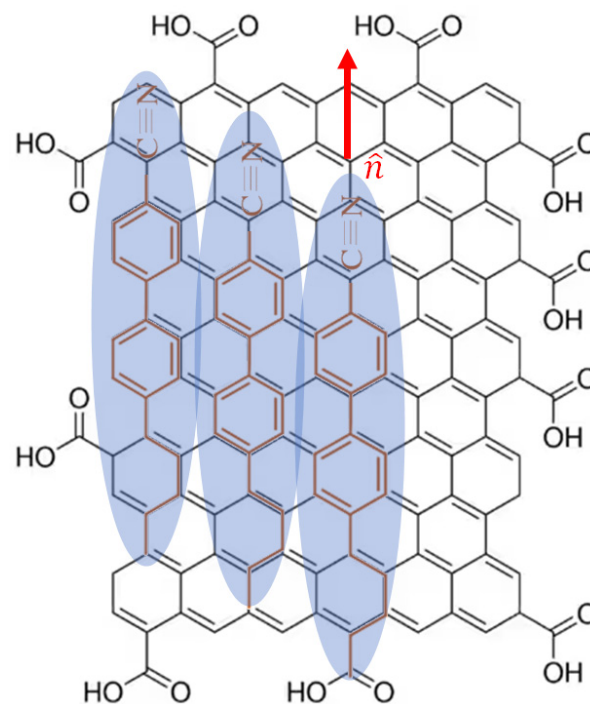


Figure 5. A schematic illustration of 5CB molecules (shown as ellipsoids) aligning on the GO's honeycomb framework due to the π - π electron stacking interaction.

The polar nature of GO's functional groups can also resonate with any polar entities within the 5CB, reinforcing the alignment. Additionally, the unique electronic properties of GO—influenced by its diverse functional groups—can initiate charge transfer interactions with 5CB molecules, promoting a distinct orientation or alignment.

We conducted similar investigations on NLC cells lacking GO thin films coated on the ITO electrodes. In these cases, we prepared standard symmetric cells with glass-ITO plates covered by formvar (Figure 6) and rubbed polyimide (Figure 7) to serve as alignment layers.

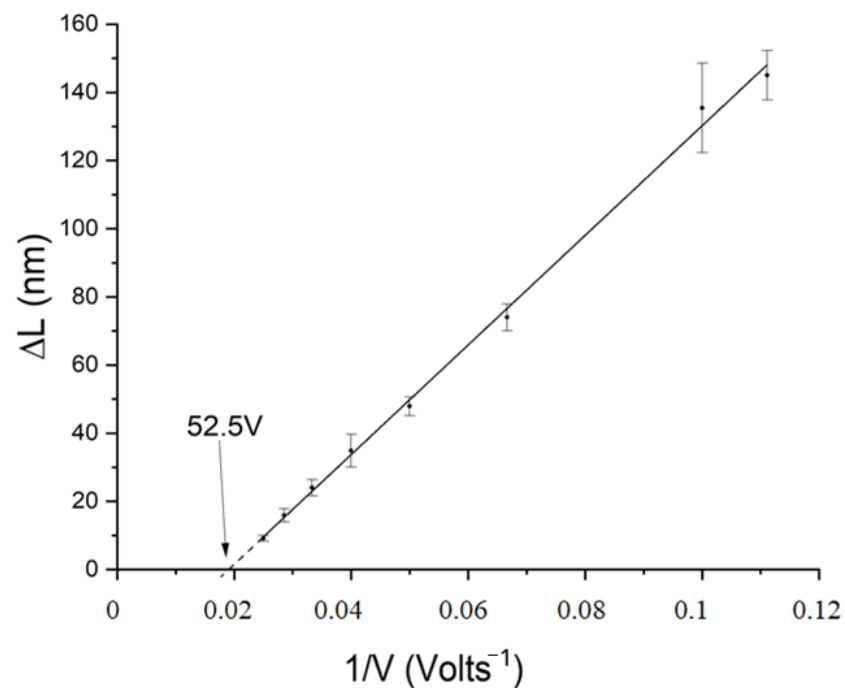


Figure 6. ΔL vs. the inverse of the applied RMS voltage in the case of the sandwich cell using Formvar[®]. The linear fit of the experimental point (solid line) and the extrapolation (dashed line) is also shown. Each experimental point is the mean value of ten measurements made on different points of the sample. The y-error bar to each experimental point of the graph represents three times the standard deviation of the mean, while the x-error bar is negligible.

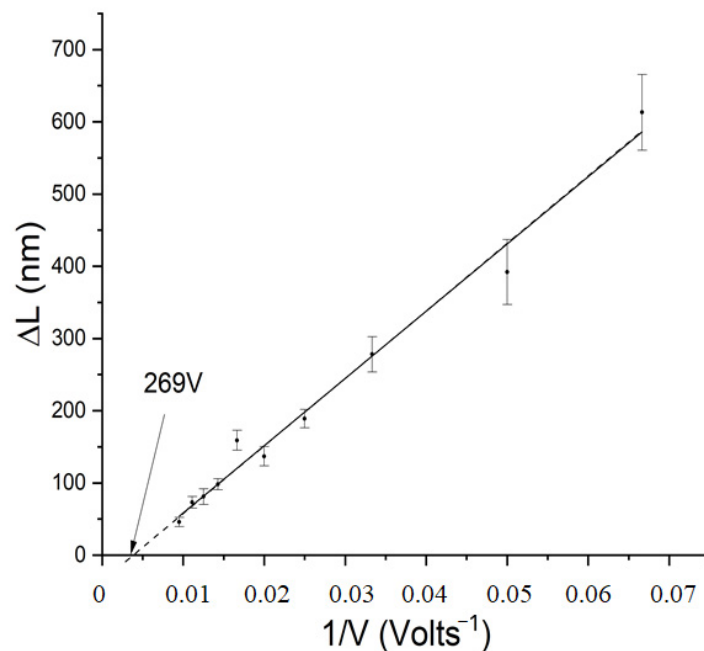


Figure 7. ΔL vs. the inverse of the applied RMS voltage in the case of the sandwich cell using polyimide. The linear fit of the experimental point (solid line) and the extrapolation (dashed line) is also shown. Each experimental point is the mean value of ten measurements made on different points of the sample. The y-error bar to each experimental point of the graph represents three times the standard deviation of the mean, while the x-error bar is negligible.

The following parameters reported in Equations (3) and (4) have been employed to calculate the anchoring energies (5).

$$\begin{cases} k_{11} = (6.3 \pm 0.1)10^{-12} \text{ N} \\ k_{22} = (4.3 \pm 0.1)10^{-12} \text{ N} \\ k_{33} = (9.6 \pm 0.1)10^{-12} \text{ N} \\ \epsilon_0 = 8.824 \cdot 10^{-12} \text{ Fm}^{-1} \\ l = (36 \pm 1)10^{-6} \text{ m} \\ \Delta\epsilon = 10.0 \pm 0.5 \end{cases} \quad (3)$$

$$\begin{cases} \text{GO} : & V_s = (348.2 \pm 0.3) \text{ V} \\ \text{Polyimide} : & V_s = (269.2 \pm 0.4) \text{ V} \\ \text{Formvar}^{\text{®}} : & V_s = (52.5 \pm 0.1) \text{ V} \end{cases} \quad (4)$$

$$\begin{cases} \text{GO} : & A = (1.7 \pm 0.1)10^{-4} \text{ Jm}^{-2} \\ \text{Polyimide} : & A = (1.3 \pm 0.1) 10^{-4} \text{ Jm}^{-2} \\ \text{Formvar}^{\text{®}} : & A = (0.26 \pm 0.03)10^{-4} \text{ Jm}^{-2} \end{cases} \quad (5)$$

We studied ten samples made under the same experimental conditions, obtaining values of anchoring energy within the margin of error of 10%. This sample-to-sample variation suggests that imperfections in the GO deposition method affected the value of the anchoring energy. For this reason, we are improving the dipping apparatus and considering a new GO deposition method.

In our investigation, the anchoring energy of GO has therefore emerged as a topic of significance, especially when contrasted with the values observed in other 2D materials, such as tin sulfide and black phosphorus [41,42]. GO's anchoring energy of $1.7 \times 10^{-3} \text{ J/m}^2$ stands out, particularly when considering the relatively lower energy of tin sulfide at $1.6 \times 10^{-6} \text{ J/m}^2$. However, when pitted against the robust anchoring energy of black phosphorus, which is approximately 0.2 J/m^2 , GO does exhibit some limitations. Still, the impressive anchoring energy of GO highlights its potential in areas where effective molecular alignment is crucial.

4. Conclusions and Outlook

Herein, a new kind of NLC cell was made using a standard sandwich configuration with the ITO electrodes covered by thin layers of GO and deposited via dip-coating.

To assess the strength of the anchorage of the 5CB molecules on GO-coated substrates, we conducted a comparative analysis with two additional cells: a polyimide cell, known for its robust anchoring energy, and a formvar cell, known for its relatively weaker anchoring energy.

Our findings demonstrate that GO surfaces induce a planar-anchoring effect in the cyanobiphenyl liquid crystal material. This confirms that, as observed in the case of graphene, it is indeed the benzene rings of the liquid crystal that coordinate with those present in the cell substrate. In contrast to the graphene deposited via CVD, the disorder introduced through dip-coating leads to non-uniform anchoring due to the presence of flakes on the substrate.

Moreover, we measured the anchoring energy using Sugimura's method, obtaining a value of $17 \times 10^{-5} \text{ J m}^{-2}$; this indicates a very strong anchoring of NLC molecules on the GO substrate and confirms the strong interaction between GO and NLC molecules.

Overall, our study provides valuable insights into the interplay between GO surfaces and liquid crystal anchoring, offering potential applications for this unique material in various technological fields. Further research is needed to explore and optimize the anchoring properties for potential practical implementations.

The interaction between NLCs and GO has garnered considerable interest, holding the promise of transformative advancements in various fields from materials science to electronics and optics.

The integration of GO into NLCs introduces a dynamic platform for tailoring optical properties. Leveraging GO's exceptional optical transparency and conductivity, researchers can manipulate light in innovative ways. Precisely controlling NLC alignment and distribution in the presence of GO will lead to opportunities for crafting advanced optical devices such as tunable lenses, adaptable beam steering mechanisms, and next-generation smart windows.

Furthermore, the profound electro-optical modulation capabilities of GO empower precise control over NLC alignment and orientation. This catalyzes the potential for swift modulation of light transmission based on external electric fields, paving the way for applications in displays, adaptive lenses, and optoelectronic switches. These devices not only promise enhanced performance but also underscore the drive toward energy-efficient technologies.

The synergy between NLCs and GO extends to the creation of multifunctional electroactive materials. Aligning NLC molecules on the surface of GO engenders materials with responsiveness to multiple stimuli, such as light, heat, and electric fields. This versatility sets the stage for advanced sensors, actuators, and adaptable textiles with applications ranging from electronics to biomedicine. The compatibility of NLCs and GO with flexible substrates positions them as frontrunners in the realm of flexible and wearable electronics. These lightweight and pliable materials, coupled with their electro-optical prowess, fuel innovation in wearable displays, conformable sensors, and flexible optoelectronic devices.

Author Contributions: Investigation, G.G.P., F.F. and C.V.; supervision, C.V.; writing—original draft preparation, G.G.P. and C.V.; writing—review and editing, G.G.P. and C.V. All authors have read and agreed to the published version of the manuscript.

Funding: This research received no external funding.

Data Availability Statement: Not applicable.

Conflicts of Interest: The authors declare no conflict of interest.

References

1. Ding, H.; Zhang, X. Sodium Intercalation in Nitrogen-Doped Graphene-Based Anode: A First-Principles Study. *Crystals* **2023**, *13*, 1011. [CrossRef]
2. Sultana, S.M.N.; Helal, E.; Gutiérrez, G.; David, E.; Moghimian, N.; Demarquette, N.R. Effect of Few-Layer Graphene on the Properties of Mixed Polyolefin Waste Stream. *Crystals* **2023**, *13*, 358. [CrossRef]
3. Sartanavičius, A.; Žemgulytė, J.; Ragulis, P.; Ratautas, K.; Trusovas, R. Laser-Induced Graphene in Polyimide for Antenna Applications. *Crystals* **2023**, *13*, 1003. [CrossRef]
4. Pianelli, A.; Kowrdziej, R.; Dudek, M.; Sielezin, K.; Olifierczuk, M.; Parka, J. Graphene-based hyperbolic metamaterial as a switchable reflection modulator. *Opt. Express* **2020**, *28*, 6708–6718. [CrossRef] [PubMed]
5. Ferrari, A.C.; Basko, D.M. Raman spectroscopy as a versatile tool for studying the properties of graphene. *Nat. Nanotechnol.* **2013**, *8*, 235–246. [CrossRef]
6. Politano, G.G.; Versace, C. Variable-Angle Spectroscopic Ellipsometry of Graphene-Based Films. *Coatings* **2021**, *11*, 462. [CrossRef]
7. Chen, D.; Feng, H.; Li, J. Graphene oxide: Preparation, functionalization, and electrochemical applications. *Chem. Rev.* **2012**, *112*, 6027–6053. [CrossRef]
8. Brisebois, P.P.; Sijaj, M. Harvesting graphene oxide—years 1859 to 2019: A review of its structure, synthesis, properties and exfoliation. *J. Mater. Chem. C* **2020**, *8*, 1517–1547. [CrossRef]
9. An, Y.-C.; Gao, X.-X.; Jiang, W.-L.; Han, J.-L.; Ye, Y.; Chen, T.-M.; Ren, R.-Y.; Zhang, J.-H.; Liang, B.; Li, Z.-L.; et al. A critical review on graphene oxide membrane for industrial wastewater treatment. *Environ. Res.* **2023**, *223*, 115409. [CrossRef]
10. Chen, Q.; Liu, L.; Zhang, A.; Wang, W.; Wang, Z.; Zhang, J.; Feng, J.; Huo, S.; Zeng, X.; Song, P. An iron phenylphosphinate@graphene oxide nanohybrid enabled flame-retardant, mechanically reinforced, and thermally conductive epoxy nanocomposites. *Chem. Eng. J.* **2023**, *454*, 140424. [CrossRef]
11. Dabrowski, B.; Zuchowska, A.; Kasprzak, A.; Zukowska, G.Z.; Brzozka, Z. Cellular uptake of biotransformed graphene oxide into lung cells. *Chem. Biol. Interact.* **2023**, *376*, 110444. [CrossRef]
12. Guo, Z.; Zhang, P.; Xie, C.; Voyiatzis, E.; Faserl, K.; Chetwynd, A.J.; Monikh, F.A.; Melagraki, G.; Zhang, Z.; Peijnenburg, W.J.G.M.; et al. Defining the Surface Oxygen Threshold That Switches the Interaction Mode of Graphene Oxide with Bacteria. *ACS Nano* **2023**, *17*, 6350–6361. [CrossRef]
13. Koo, D.; Sung, J.; Suh, H.; Bae, S.; So, H. Comprehensive analysis of CNT/NS/GO composites: Dispersion effect of graphene oxide for environmental sensor application. *Compos. Part A Appl. Sci. Manuf.* **2023**, *173*, 107639. [CrossRef]

14. Li, Y.; Hao, Z.; Cao, H.; Wei, S.; Jiao, T.; Wang, M. Study on annealed graphene oxide nano-sheets for improving the surface enhanced fluorescence of silver nanoparticles. *Opt. Laser Technol.* **2023**, *160*, 109054. [[CrossRef](#)]
15. Taheriazam, A.; Abad, G.G.Y.; Hajimazdarany, S.; Imani, M.H.; Ziaolhagh, S.; Zandieh, M.A.; Bayanzadeh, S.D.; Mirzaei, S.; Hamblin, M.R.; Entezari, M.; et al. Graphene oxide nanoarchitectures in cancer biology: Nano-modulators of autophagy and apoptosis. *J. Control. Release* **2023**, *354*, 503–522. [[CrossRef](#)] [[PubMed](#)]
16. Vasseghian, Y.; Sezgin, D.; Nguyen, D.C.; Hoang, H.Y.; Yilmaz, M.S. A hybrid nanocomposite based on CuFe layered double hydroxide coated graphene oxide for photocatalytic degradation of trimethoprim. *Chemosphere* **2023**, *322*, 138243. [[CrossRef](#)] [[PubMed](#)]
17. Wu, J.; Lin, H.; Moss, D.J.; Loh, K.P.; Jia, B. Graphene oxide for photonics, electronics and optoelectronics. *Nat. Rev. Chem.* **2023**, *7*, 162–183. [[CrossRef](#)] [[PubMed](#)]
18. Zou, Y.; Wang, W.; Wang, H.; Pan, C.; Xu, J.; Pozdnyakov, I.P.; Wu, F.; Li, J. Interaction between graphene oxide and acetaminophen in water under simulated sunlight: Implications for environmental photochemistry of PPCPs. *Water Res.* **2023**, *228*, 119364. [[CrossRef](#)]
19. Aboutalebi, S.H.; Gudarzi, M.M.; Zheng, Q.B.; Kim, J.-K. Spontaneous Formation of Liquid Crystals in Ultralarge Graphene Oxide Dispersions. *Adv. Funct. Mater.* **2011**, *21*, 2978–2988. [[CrossRef](#)]
20. Shim, Y.H.; Kim, S.Y. Continuous structural deformation of graphene oxide liquid crystal colloids under shear for hydrogel films. *Carbon* **2023**, *202*, 358–367. [[CrossRef](#)]
21. Abedin, M.J.; Gamot, T.D.; Martin, S.T.; Ali, M.; Hassan, K.I.; Mirshekarloo, M.S.; Tabor, R.F.; Green, M.J.; Majumder, M. Graphene Oxide Liquid Crystal Domains: Quantification and Role in Tailoring Viscoelastic Behavior. *ACS Nano* **2019**, *13*, 8957–8969. [[CrossRef](#)]
22. Gelbart, W.M. Molecular theory of nematic liquid crystals. *J. Phys. Chem.* **1982**, *86*, 4298–4307. [[CrossRef](#)]
23. Strangi, G.; Versace, C.; Scaramuzza, N. Surface anchoring energy modulation in liquid crystal cells with mixed conductor boundary layers. *Appl. Phys. Lett.* **2001**, *78*, 2455–2457. [[CrossRef](#)]
24. Bisoyi, H.K.; Li, Q. Liquid Crystals: Versatile Self-Organized Smart Soft Materials. *Chem. Rev.* **2022**, *122*, 4887–4926. [[CrossRef](#)] [[PubMed](#)]
25. Basu, R.; Kinnamon, D.; Garvey, A. Graphene and liquid crystal mediated interactions. *Liq. Cryst.* **2016**, *43*, 2375–2390. [[CrossRef](#)]
26. Basu, R. Graphene as an alignment agent, an electrode, and a source of surface chirality in a smectic-A liquid crystal. *Phys. Rev. E.* **2021**, *103*, 22710. [[CrossRef](#)]
27. Basu, R.; Shalov, S.A. Graphene as transmissive electrodes and aligning layers for liquid-crystal-based electro-optic devices. *Phys. Rev. E* **2017**, *96*, 12702. [[CrossRef](#)] [[PubMed](#)]
28. Yu, J.-S.; Ha, D.-H.; Kim, J.-H. Mapping of the atomic lattice orientation of a graphite flake using macroscopic liquid crystal texture. *Nanotechnology* **2012**, *23*, 395704. [[CrossRef](#)] [[PubMed](#)]
29. Kim, D.W.; Kim, Y.H.; Jeong, H.S.; Jung, H.-T. Direct visualization of large-area graphene domains and boundaries by optical birefringency. *Nat. Nanotechnol.* **2012**, *7*, 29–34. [[CrossRef](#)] [[PubMed](#)]
30. Shehzad, M.A.; Tien, D.; Waqas Iqbal, M.; Eom, J.; Park, J.; Hwang, C.; Seo, Y. Nematic Liquid Crystal on a Two Dimensional Hexagonal Lattice and its Application. *Sci. Rep.* **2015**, *5*, 13331. [[CrossRef](#)]
31. Lim, Y.; Lee, B.; Kwon, Y.; Choi, Y.; Murali, G.; Lee, J.; Nguyen, V.L.; Lee, Y.H.; Lee, S. Monitoring defects on monolayer graphene using nematic liquid crystals. *Opt. Express* **2015**, *23*, 14162. [[CrossRef](#)] [[PubMed](#)]
32. Basu, R.; Lee, A. Ion trapping by the graphene electrode in a graphene-ITO hybrid liquid crystal cell. *Appl. Phys. Lett.* **2017**, *111*, 161905. [[CrossRef](#)]
33. Basu, R.; Atwood, L.J. Characterizations of a graphene-polyimide hybrid electro-optical liquid crystal device. *OSA Contin.* **2019**, *2*, 83–91. [[CrossRef](#)]
34. Son, S.-R.; An, J.; Choi, J.-W.; Kim, S.; Park, J.; Lee, J.H. Surface-anchored alkylated graphene oxide as a two-dimensional homeotropic alignment layer for nematic liquid crystals. *Mater. Today Commun.* **2021**, *28*, 102539. [[CrossRef](#)]
35. Maximean, D.M. New grafted ferrite particles/liquid crystal composite under magnetic field. *J. Magn. Magn. Mater.* **2018**, *452*, 343–348. [[CrossRef](#)]
36. Du, Y.; Tian, H.; Cui, X.; Wang, H.; Zhou, Z.-X. Electrically tunable liquid crystal terahertz phase shifter driven by transparent polymer electrodes. *J. Mater. Chem. C* **2016**, *4*, 4138–4142. [[CrossRef](#)]
37. Kowerdziej, R.; Krupka, J.; Nowinowski-Kruszelnicki, E.; Olifierczuk, M.; Parka, J. Microwave complex permittivity of voltage-tunable nematic liquid crystals measured in high resistivity silicon transducers. *Appl. Phys. Lett.* **2013**, *102*, 102904. [[CrossRef](#)]
38. Nehring, J.; Kmetz, A.R.; Scheffer, T.J. Analysis of weak-boundary-coupling effects in liquid-crystal displays. *J. Appl. Phys.* **2008**, *47*, 850–857. [[CrossRef](#)]
39. Sugimura, A.; Miyamoto, T.; Tsuji, M.; Kuze, M. Determination of the unified surface-anchoring energy of a nematic liquid crystal on a polymer substrate. *Appl. Phys. Lett.* **1998**, *72*, 329–331. [[CrossRef](#)]
40. Dreyer, D.R.; Park, S.; Bielawski, C.W.; Ruoff, R.S. The chemistry of graphene oxide. *Chem. Soc. Rev.* **2010**, *39*, 228–240. [[CrossRef](#)] [[PubMed](#)]

41. Solodar, A.; Alzaidy, G.; Huang, K.C.-C.; Hewak, D.; Abdulhalim, I. Transition Metal Chalcogenide Tin Sulfide Nanodimensional Films Align Liquid Crystals. *arXiv* **2018**, arXiv:1802.01401.
42. Kim, D.W.; Jeong, H.; Kwon, K.; Ok, J.M.; Kim, S.M.; Jung, H. Ultrastrong Anchoring on the Periodic Atomic Grooves of Black Phosphorus. *Adv. Mater. Interfaces* **2016**, *3*, 1600534. [[CrossRef](#)]

Disclaimer/Publisher's Note: The statements, opinions and data contained in all publications are solely those of the individual author(s) and contributor(s) and not of MDPI and/or the editor(s). MDPI and/or the editor(s) disclaim responsibility for any injury to people or property resulting from any ideas, methods, instructions or products referred to in the content.